

Opening the Band Gap of Graphene via Fluorination for High-Performance Dual-Mode Photodetector Application

Ji-Yu Xu,^{†,§} Ju-Song Yu,^{†,§} Ji-Hai Liao,^{*,‡} Xiao-Bao Yang,^{‡,ID} Chun-Yan Wu,^{*,†} Yi Wang,[†] Li Wang,[†] Chao Xie,^{*,†,ID} and Lin-Bao Luo^{*,†,ID}

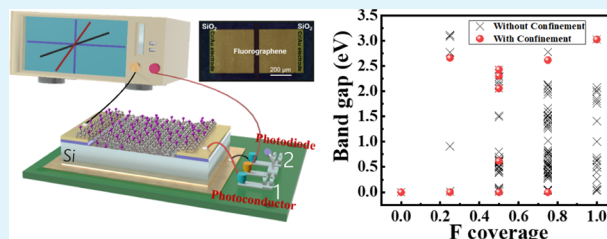
[†]School of Electronic Science and Applied Physics, Hefei University of Technology, Hefei, Anhui 230009, China

[‡]Department of Physics, South China University of Technology, Guangzhou 510640, Guangdong, China

Supporting Information

ABSTRACT: Fluorination is an effective process to open the band gap of graphene (Gr), which is beneficial to the development of optoelectronic devices working in wide wavelength. Herein, we report a dual-mode broadband photodetector (PD) by integrating fluorinated graphene (F-Gr) with silicon (Si). It is found that when working in photoconductive mode, the F-Gr/Si heterojunction exhibited a remarkable photoresponse over a wide spectral region from ultraviolet (UV), visible to near infrared (NIR) light with a high responsivity (R) of 1.9×10^7 A W^{-1} and specific detectivity (D^*) of 4.4×10^{12} Jones at 650 nm. Nonetheless, both parameters will be considerably reduced when the F-Gr/Si heterojunction works in the photodiode mode. In this mode, the $I_{\text{light}}/I_{\text{dark}}$ ratio is as high as 2.0×10^5 and the response speed is accelerated by more than 3 orders of magnitude from about 5 ms to 6.3 μ s. Notably, the responsivity of the device in the UV and NIR regions was remarkably enhanced in comparison with that of pristine Gr/Si-heterojunction-based devices. Considering the F-coverage-dependent band gap of the F-Gr revealed by the first-principle calculations, we believe that the enhancement was ascribed to the opening of the band gap in the partially fluorinated Gr, which is stabilized due to the configuration entropy as the temperature increases. The dual-mode PD enabled the simultaneous weak light detection and fast photodetection, which overcome the limitation of the traditional monomode PD.

KEYWORDS: fluorinated graphene, band gap opening, photoconductive photodetector, photodiode, broadband



INTRODUCTION

Since its first discovery in 2004, graphene (Gr) has attracted explosive research interest from both academia and industry.¹ With its broad light absorption,² high carrier mobility ($\sim 200\,000$ cm² V⁻¹ s⁻¹ at room temperature), and short carrier lifetime,^{3,4} Gr has demonstrated exciting potential for assembling various optoelectronic devices, such as broadband high-speed photodetectors (PDs),⁵ solar cells,⁶ light modulator,⁷ and fiber laser.⁸ However, in spite of the high absorption coefficient, the intrinsically weak light absorption ($\sim 2.3\%$ for pristine Gr) due to the short light–matter interaction length is insufficient for light-harvesting device applications.⁹ Moreover, the short photocarrier lifetime resulting from its gapless nature also leads to fast carrier recombination,^{10,11} which limits the efficient generation of photocurrent or photovoltage.

Tremendous efforts have been focused on inducing a finite band gap in Gr. McCann et al. demonstrated the gap opening of the bilayer Gr with a maximum value of 130 meV in 2006 by applying a strong perpendicular electric field.¹² Another effective approach was to reduce the dimensionality of a two-dimensional (2D) Gr to one-dimensional confined Gr superstructure such as Gr nanoribbons.^{13–16} Unfortunately, the opened gap was inversely proportional to the width of the superstructure. That means, to achieve a substantial gap of

about 0.5 eV, the width of Gr needs to be 2–3 nm, which was greatly limited by the current photolithographic techniques. Chemical doping has proved to be a facile and effective approach to open up the band gap of Gr and tune its electronic properties.¹⁷ By introducing specific heteroatoms (boron,¹⁸ nitrogen,¹⁹ fluorine,^{20,21} chlorine,²² sulfur,²³ etc.), the graphitic carbon atoms will be replaced or covalently bonded by foreign atoms. The trigonal sp² symmetry hybrid orbital of the carbon atoms in Gr unit cell is broken, giving rise to a different potential on the two carbon atoms and therefore opening up the gap.²⁴

Fluorinated graphene (F-Gr) is an important graphene derivative.^{25,26} To date, many methods have been developed for the synthesis of F-Gr. For example, Nair et al. obtained a stoichiometric derivative by exposing Gr to a fluorinating agent XeF₂. The resultant F-Gr was an excellent insulator with high thermal and chemical stability, which can be used as an atomically thin insulator or a tunnel barrier in Gr-based heterostructures.²¹ By using a controllable SF₆ plasma treatment in a reactive ion etching (RIE) system, Sun and

Received: March 15, 2019

Accepted: May 23, 2019

Published: May 23, 2019

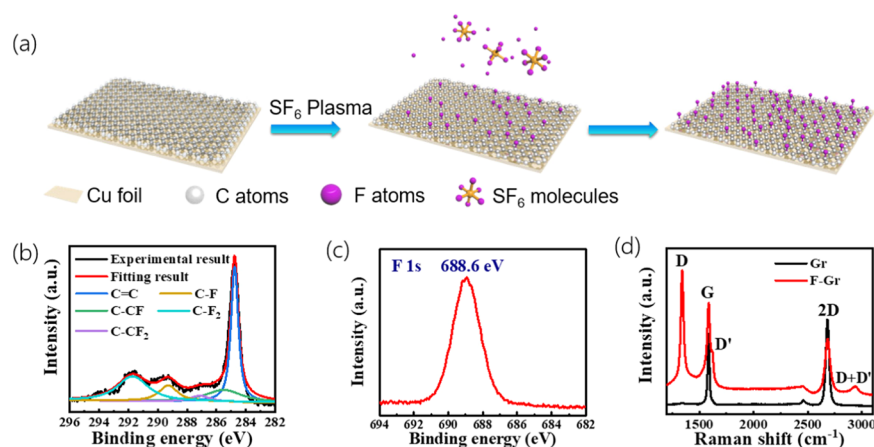


Figure 1. (a) Schematic diagram showing the fluorination process. High-resolution XPS spectra of F-Gr: C 1s (b) and F 1s (c) spectrum. (d) Raman spectra of both intrinsic Gr and F-Gr.

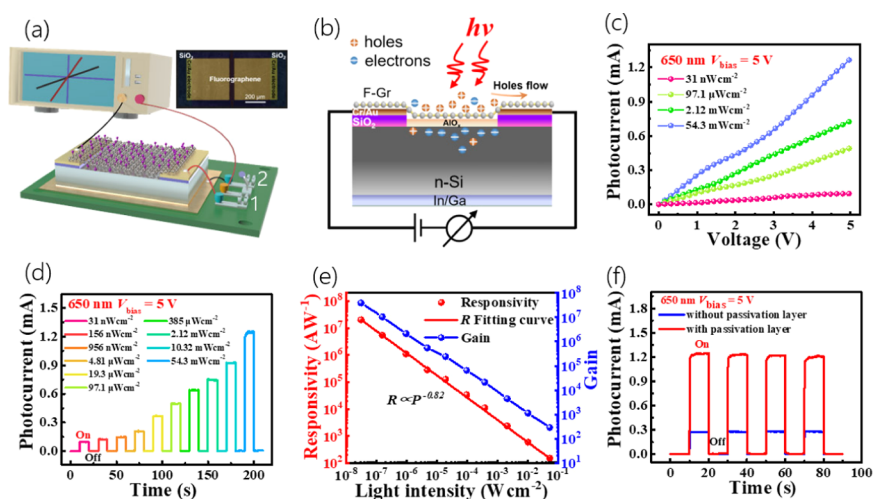


Figure 2. (a) Schematic diagram of the F-Gr/Si dual-mode PD, the inset shows the pseudo-colored field-emission scanning electron microscopy (FESEM) image of a typical device. (b) Schematic structure of the F-Gr/Si photoconductive PD. (c) I - V curves under 650 nm light illumination with varied light intensities. (d) Time response under 650 nm light illumination with varied light intensities. (e) Responsivity and photoconductive gain as a function of the incident light intensity. (f) Photocurrent of the photoconductive detectors with and without passivation.

colleagues realized the fluorination of a monolayer chemical vapor deposition (CVD)-grown Gr, which can be used for sensitive ammonia gas detection.²⁷ Moreover, Yang's group found that F-Gr can also be fabricated by SF_6 plasma treatment in an inductively coupled plasma system.²⁸ By using the F-Gr as an insulator interlayer, they achieved a high power conversion efficiency solar cell due to suppressed carrier recombination at the front surface of Si. Very recently, Hu et al. reported the broadband photodetection of the F-Gr/Gr van der Waals heterostructures, which was attributed to the synergistic effects of the spatial nonuniform collective quantum confinement of sp^2 domains and the trapping of photoexcited charge carriers in the localized states in sp^3 domains.²⁹ However, the responsivity and response speed of the F-Gr/Gr PD still need to be further improved.

Herein, we reported on the fluorination of CVD-grown Gr by plasma treatment approach. By combining F-Gr with Si, we achieved F-Gr/Si heterojunction device, which showed broadband photodetection and can work as both a photoconductive PD and a photodiode PD. In the first operation mode, the F-Gr/Si device showed excellent weak light detection ability over the broadband spectral region from

deep ultraviolet (DUV), visible to near infrared (NIR), giving a high responsivity (R) of $1.9 \times 10^7 \text{ A W}^{-1}$ under 650 nm light illumination. Meanwhile, the F-Gr/Si heterojunction shows an obvious photovoltaic behavior, which can work as a self-powered broadband photodiode. This operation mode leads to an $I_{\text{light}}/I_{\text{dark}}$ ratio of 10^5 and a fast response speed (τ_r/τ_f) of $6.3/9.7 \mu\text{s}$ at 650 nm light illumination. The first-principle calculations revealed the F coverage-dependent band gap of the F-Gr, which can account for the remarkable enhancement of responsivity in the UV and NIR region. This dual-mode PD enables the simultaneous weak light detection and fast photodetection, which overcomes the limitation of the traditional monomode PD.

RESULTS AND DISCUSSION

The F-Gr was synthesized by directly fluorinating chemical vapor deposition (CVD)-grown Gr in an RIE system using SF_6 as the etching gas (Figure 1a). The covalent C-F bonds in F-Gr can be confirmed by X-ray photoelectron spectroscopy (XPS). By dividing the C 1s peak in Figure 1b, totally five independent peaks with binding energies at 291.7, 289.3, 287.1, 285.6, and 284.4 eV, due to C-F₂, C-F, C-CF₂, C-

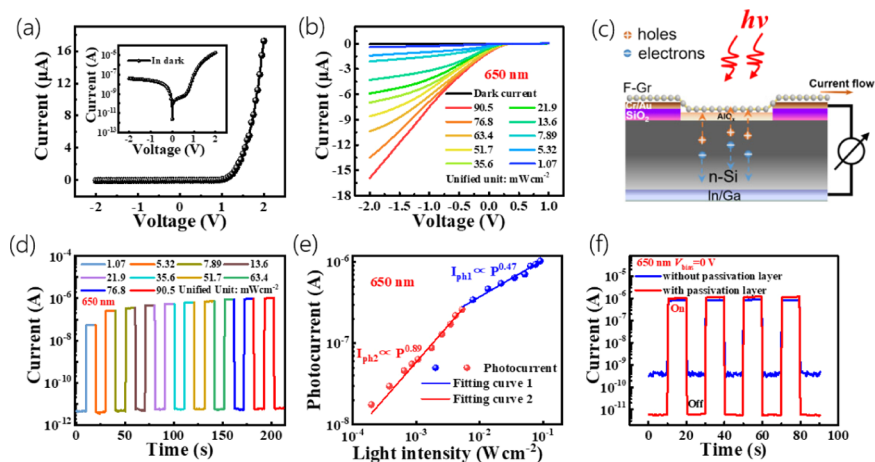


Figure 3. (a) I – V curve of the F-Gr/Si photodiode in the dark, the inset is shown in the semilogarithmic scale. (b) I – V curves under 650 nm light illumination with varied light intensities. (c) Schematic structure of the device working in the photodiode mode. (d) Photoresponse under 650 nm light illumination with varied light intensities. (e) Photocurrent as a function of the incident light intensity at zero bias. (f) Photoresponse of the photodiode with and without passivation.

CF, and C=C bonds, respectively, were observed.²⁷ Meanwhile, the high-resolution F 1s spectrum at 688.6 eV (Figure 1c) can be assigned to the C–F covalent bond, which further verifies that RIE treatment in the SF₆ plasma can break pristine C=C sp² bonds and form C–F sp³ covalent bonds.³⁰ Raman spectrum of the Gr in Figure 1d shows signature G peak at ~1588 cm⁻¹ and 2D peaks at 2687 cm⁻¹ with an intensity ratio $I_{2D}/I_G \approx 1$, revealing the nature of a bilayer Gr.³¹ The weak intensity of D and D' peaks indicated that few defects existed in Gr.³² Once treated with SF₆, disorder-induced D peak (~1343 cm⁻¹) and D' peak (~1622 cm⁻¹) appeared in the Raman spectrum, which represented internal scattering and intravalley scattering, respectively.³³ Moreover, obvious D + D' peak appeared at 2941 cm⁻¹, which was a characteristic peak of the two-phonon defect processes and also proves that many defects have been induced in F-Gr.³⁴ According to the calculation based on eq 1³⁵

$$n_D(\text{cm}^{-2}) = \frac{(1.8 \pm 0.5) \times 10^{22} \left(\frac{I_D}{I_G} \right)}{\lambda_L^4} \quad (1)$$

the defect density n_D in F-Gr ranged from 2.2×10^{11} to 4.0×10^{11} cm⁻², which was about one order of magnitude higher than that of the CVD-grown Gr (ranging from 1.7×10^{10} to 3.0×10^{10} cm⁻²). Further comparison of current (I)–voltage (V) curves of both Gr and F-Gr in dark shows that after fluorine doping (Figure S1), the resistivity was increased by around 30%, indicative of successful fluorination.

To study the photoelectrical property of the F-Gr, a F-Gr/Si heterojunction PD with dual operation modes was assembled (Figure 2a). Figure S2 shows the detailed schematic process in which an AlO_x passivation layer with a thickness of 3.6 nm was deposited at the F-Gr/Si interface (Figure S3), followed by the transfer of F-Gr onto Si wafer. In this study, the dual-mode photodetection was realized by a single-pole double-throw switch. When the switch was turned to end 1, the bias was applied on the two Cr/Au electrodes and F-Gr/Si heterojunction worked as a photoconductor. However, when switch was turned to end 2, the bias was applied on the bottom In/Ga electrode and one Cr/Au electrode, and the F-Gr/Si heterojunction will operate in the photodiode mode. Figure 2b shows the operation principle of the F-Gr/Si heterojunction

photoconductive PD. A built-in electric field (depletion region) will be formed at the interface of F-Gr/Si heterojunction. When illuminated by light with photoenergy higher than the band gaps, the photogenerated electron–hole pairs in the depletion region will be separated in opposite directions. The photogenerated holes in Si were swept into F-Gr and the photogenerated electrons in F-Gr were swept into Si. Driven by the external bias, the holes transferred fast and recirculated multiple times before recombining in the charge transport channel F-Gr, giving rise to a high photocurrent gain.³⁶ The optoelectronic characterization in the photoconductive mode was then measured under the illumination of 650 nm light with different light intensities, and the photocurrent (I_{ph})–voltage (V) curves are shown in Figure 2c. It can be clearly found that the photocurrent was dependent on the incident light intensity. With the incident power ranging from 31 nW cm⁻² to 54.3 mW cm⁻², it increased from 0.09 to 1.24 mA at the applied voltage of 5 V. This is reasonable, since stronger illumination will generate more photon-excited electron–hole pairs and therefore lead to higher photocurrent. Figure 2d plots the time-dependent photoresponse of the device under different light intensities. Apparently, the device can be reversibly switched between low- and high-conductance states. Notably, even when the incident light intensity was down to 31 nW cm⁻², the device can still have a photocurrent of 94.8 μA, suggesting the possibility of the F-Gr/Si for weak light detection. By deducing the photoresponse curve in Figure S4, the rise and fall time (τ_r/τ_f) in the photoconductive mode were estimated to be 5.2/5.9 ms, respectively.

To further evaluate the PD, responsivity (R) and photoconductive gain (G) were calculated following the equations³⁷

$$R(\text{AW}^{-1}) = \frac{I_{ph}}{P_{in}S} = \eta \left(\frac{q\lambda}{hc} \right) G \quad (2)$$

where I_{ph} is the current under 650 nm illumination, P_{in} is the incident light intensity, S is the effective device area, η is the quantum efficiency, q is the elementary electron charge (1.6×10^{-19} C), λ is the incident light wavelength, h is the Planck's constant, and c is speed of light in vacuum. As plotted in Figure 2e, the responsivity (R) and the photoconductive gain (G)

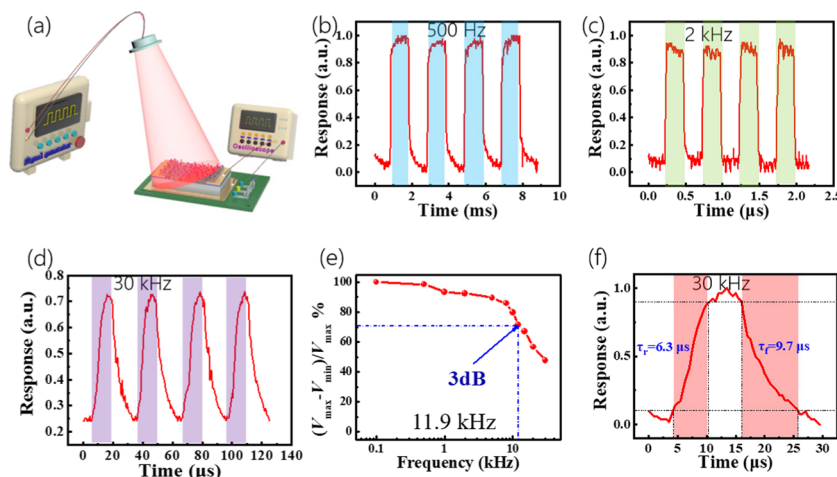


Figure 4. (a) Schematic illustration for the measurement of the photoresponse. (b–d) Response of the F-Gr/Si photodiode PD upon pulsed light irradiation at frequencies of 500 Hz, 2 kHz, and 30 kHz, respectively. (e) Relative balance $(V_{\max} - V_{\min})/V_{\max}$ versus switching frequency, showing the 3 dB bandwidth of about 11.9 kHz. (f) A single magnified photoresponse curve at the frequency of 30 kHz to calculate the response time.

decreased with the increase of the incident light intensity, which was consistent with previous report.³⁸ Surprisingly, the responsivity and gain can reach as high as 1.9×10^7 A W⁻¹ and 3.9×10^7 under the light intensity of 31 nW cm^{-2} , which may be attributed to the ultrafast transition of carriers within F-Gr as well as the large recombination time scale arising from the built-in field.³⁹ As we know that due to the excellent transmittance of F-Gr, both F-Gr and Si can work as light absorbers at the wavelength of 650 nm. The photogenerated holes in Si are injected into F-Gr by the built-in field, while the photogenerated electrons in F-Gr are swept into Si, which greatly lowered the recombination ratio and prolonged the lifetime of the photogenerated carriers. In addition to R and G , the specific detectivity (D^*) was also calculated by noise equivalent power (NEP)³⁷

$$\text{NEP} = \frac{i_n^{2/2}}{R} \quad (3)$$

$$D^* = \frac{(SB)^{1/2}}{\text{NEP}} \quad (4)$$

where $i_n^{2/2}$ is the root mean square value of the noise current, S is the effective area, and B is the specific bandwidth. As shown in Figure S5, the noise spectral density of the photoconductive PD was $5.3 \times 10^{-8} \text{ A Hz}^{-1/2}$ at the bandwidth of 1 Hz. Therefore, the highest specific detectivity D^* at 650 nm was calculated to be 4.4×10^{12} Jones. It should be pointed out that the passivation layer played an important role in achieving the high responsivity and the on/off ratio. After passivating, the density of dangling bonds and defect states at the Si surface will be greatly reduced. Therefore, the recombination activities at the Si surface will be suppressed and more photogenerated carriers will be collected, giving rise to the increase of photocurrent by about 3-folds.⁴⁰

Once the operation mode is switched to photodiode one, the F-Gr/Si heterojunction device will display a remarkable rectification behavior in the dark, with a rectification ratio of 460 at $\pm 2 \text{ V}$ (Figure 3a). Given the Ohmic contact formed at both F-Gr/Cr/Au and n-Si/In/Ga interfaces, the rectification characteristic shall be ascribed to the F-Gr/Si heterojunction. Careful observation of the I - V curves shows that the device

actually exhibits obvious photovoltaic behavior when illuminated by 650 nm incident light (Figure 3b), giving a maximum open-circuit voltage (V_{OC}) of about 0.4 V. As we mentioned above, the photogenerated electrons (holes) will be rapidly separated by the built-in electric field toward Si (F-Gr), and subsequently extracted by In:Ga (Cr/Au) electrode, leading to the photocurrent at zero bias and rendering the F-Gr/Si heterojunction a self-powered PD (Figure 3c). Figure 3d illustrates the photoresponse characteristics of the F-Gr/Si heterojunction photodiode under 650 nm light illumination of different light intensities. Similarly, the photocurrent of the F-Gr/Si photodiode was observed to increase gradually with the increasing light intensity from 1.07 to 90.5 mW cm^{-2} . Specifically, the on/off ratio reaches the highest value of 2.0×10^5 at the intensity of 90.5 mW cm^{-2} . The relationship between photocurrent and light intensity can be fitted with a power law $I_{\text{ph}} \propto P^\theta$, where θ is an exponent and is determined by the linear relationship of light intensity and photocurrent. As plotted in Figure 3e, in the lower light intensity range (from $198 \mu\text{W cm}^{-2}$ to 5.3 mW cm^{-2}), θ was fitted to be 0.89. While in the higher light intensity range (from 7.9 to 90.5 mW cm^{-2}), θ was fitted to 0.47. The relatively large θ at low light intensity is probably due to the lower recombination possibility.⁴¹ Moreover, the deviation of θ from the integer may be attributed to the existence of trap states. Note that, in the photodiode mode, the AlO_x passivation layer can act as a barrier to prevent the transport of electron, which can substantially reduce the dark current, leading to at least one order of magnitude increase in the on/off ratio (Figure 3f). By employing eqs 2–4 and the noise current in Figure S6, the responsivity and specific detectivity of the F-Gr/Si photodiode at an intensity 1.07 mW cm^{-2} were calculated to be 334 mA W^{-1} and 2.3×10^{11} Jones, respectively. Moreover, the external quantum efficiency (EQE) of the device was estimated to be 63.8% (please see the Supporting Information), which was comparable to that of the Gr/Si photodiode.⁴²

Another advantageous feature of the F-Gr/Si heterojunction device in the photodiode mode is the fast response speed, which was recorded by shining the device with high-frequency light irradiation (Figure 4a). Figure 4b–d shows the transient photoresponse at different frequencies from 500 Hz, 2 kHz to 30 kHz. It can be clearly seen that the device can be reversibly

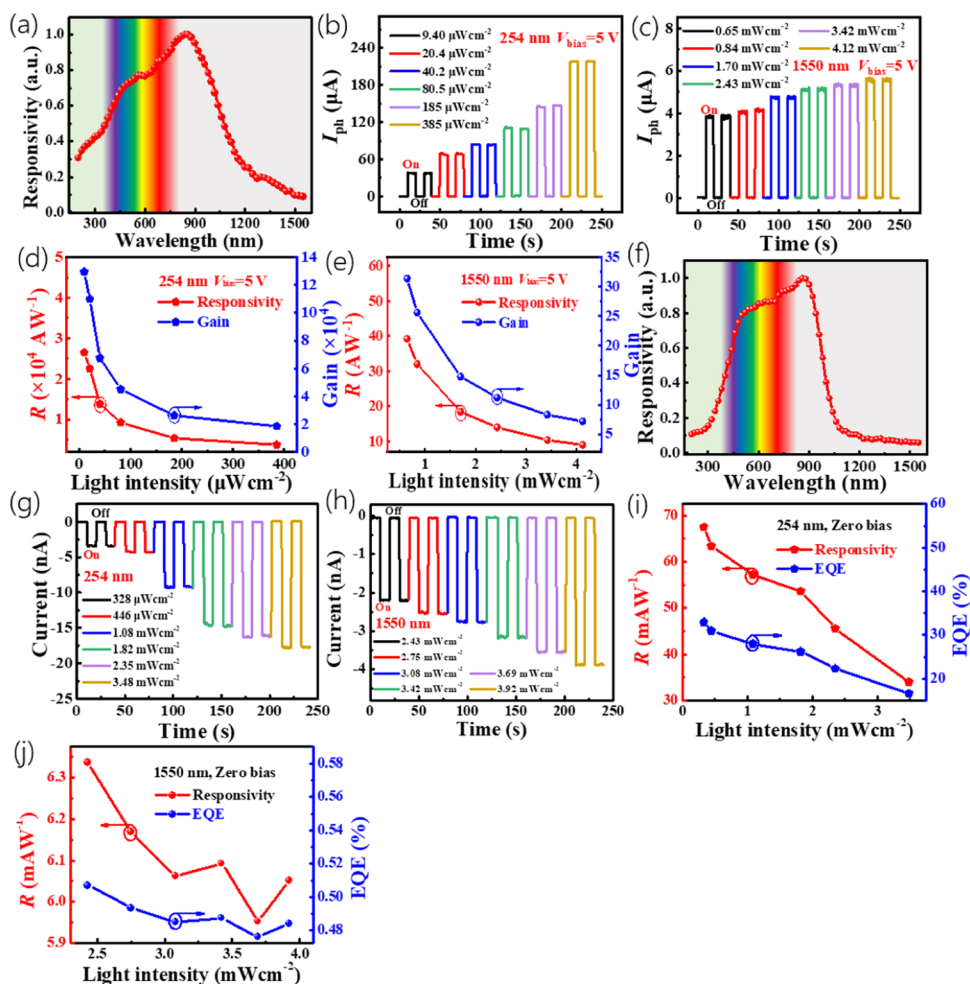


Figure 5. (a) Spectral response of the F-Gr/Si photoconductive detector in the range 200–1550 nm. Photoresponse of the photoconductive detector under 254 nm (b) and 1550 nm (c) light illumination with varied light intensities. Responsivity and gain of the F-Gr/Si photoconductive detector under (d) 254 nm and (e) 1550 nm illumination with different intensities. (f) Spectral response of the F-Gr/Si photodiode in the range 200–1550 nm. Photoresponse of the photodiode under 254 nm (g) and 1550 nm (h) light illumination with varied light intensities. Responsivity and EQE of the F-Gr/Si photodiode detector under (i) 254 nm and (j) 1550 nm illumination with different intensities.

switched between high- and low-conductance states with good reproducibility for all switching frequencies. According to the relative balance as a function of frequency shown in Figure 4e, the 3 dB bandwidth can be deduced to be about 11.9 kHz, suggesting that the F-Gr/Si PD can work properly over a wide switching frequency range. To extract the response speed of the F-Gr/Si photodiode, a single magnified cycle at the frequency of 30 kHz is plotted in Figure 4f, from which the rise time (τ_r) and the fall time (τ_f) were estimated to be about 6.3 and 9.7 μ s, respectively.

More importantly, the F-Gr/Si heterojunction device in both operation modes shows obvious sensitivity to both DUV and NIR illumination (Figure 5a). For instance, when the F-Gr/Si heterojunction in the photoconductive mode was shined by 254 or 1550 nm light, the device can be reversibly switched between high- and low-conductance states and the photocurrent (I_{light}) increased accordingly with increasing incident light intensity (Figure 5b,c). The responsivity and photoconductive gain for 254 nm illumination are estimated to be 2.6×10^4 A W $^{-1}$ and 1.3×10^5 , respectively (Figure 5d). Comparatively, the photocurrent under 1550 nm illumination was dramatically reduced by about 2 orders of magnitude. The responsivity and photoconductive gain were 39.2 A W $^{-1}$ and

31, respectively (Figure 5e). As a matter of fact, similar photoresponse to DUV and NIR light was also observed in the photodiode mode (Figure 5f–h). The responsivity and EQE were 68 mA W $^{-1}$ and 33% for 254 nm illumination and 6.34 mA W $^{-1}$ and 0.48% for 1550 nm illumination (Figure 5i–j), suggesting the potential application of the current F-Gr/Si heterojunction device for broadband detection.

To systematically evaluate the device performance of the present F-Gr/Si heterojunction PD and to reveal the difference in the photoelectrical properties between intrinsic Gr and F-Gr, a controlled device composed of Gr/Si heterojunction was also fabricated. Figure S7a,b compares the photoresponse of both F-Gr/Si and Gr/Si heterojunctions under the same illumination, respectively. In both photoconductive and photodiode modes, the photocurrent of F-Gr/Si is close to that of Gr/Si. To our surprise, both devices are widely divergent on photoresponse in the UV and NIR regions. Figure 6a,b compares the responsivity of the photoconductive PDs shined by both 254 and 1550 nm. One can see that the responsivity of F-Gr/Si has been enhanced by about 48% from an average value of $(4.4\text{--}6.5) \times 10^3$ A W $^{-1}$ in the wavelength range of 200–300 nm, while the enhancement is about 30-folds in the NIR region (1300–1500 nm). As for the

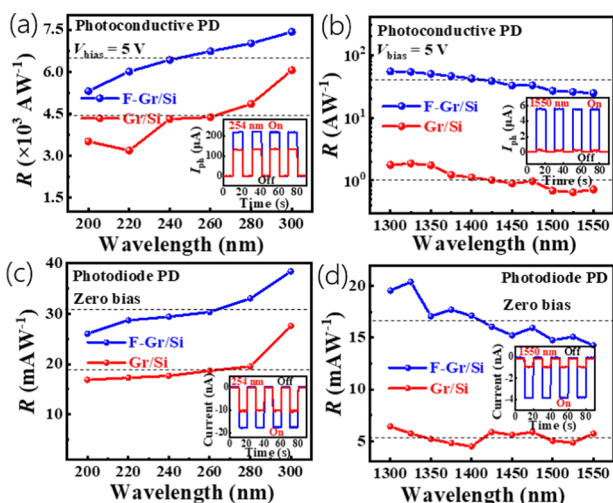


Figure 6. Responsivity of the photoconductive detector in the range of 200–300 nm (a) and 1300–1550 nm (b). Responsivity of the photodiode detectors in the range of 200–300 nm (c) and 1300–1550 nm (d), all the insets show the $I-t$ curves upon 254 nm light illumination with the intensity of $385 \mu\text{W cm}^{-2}$ or 1550 nm light illumination with the intensity of 4.12 mW cm^{-2} , respectively.

photodiode devices, the responsivity is reasonably low due to the absence of impact ionization and carrier multiplication. However, an enhancement of about 2-folds can still be observed when the PD was illuminated by UV and NIR incident light (Figure 6c,d). Considering the fact that planar Si shows an absorption edge of about 1100 nm and weak photoresponse to UV light with wavelength less than 400 nm, the enhanced photoresponse of the F-Gr/Si device should be exclusively ascribed to the contribution from F-Gr.

Table 1 summarizes the key metrics of our dual-mode F-Gr/Si PD including the on/off ratio, responsivity, specific detectivity, and response time with other PDs assembled from F-Gr or Gr. It can be concluded that the response speed of the dual-mode F-Gr/Si device is comparable to the Gr- or F-Gr-based photodetector with the same operation mode. However, the F-Gr/Si photoconductive PD has the highest responsivity of $1.9 \times 10^7 \text{ A W}^{-1}$ under visible light illumination, which is at least 3 orders of magnitude higher

than that of the Gr/Si photoconductive PD and the F-Gr/Gr field-effect transistor PD. On the other hand, our F-Gr/Si photoconductive PD has a specific detectivity of 4.4×10^{12} Jones, such a value is slightly lower than that of the Gr/Si photodiode,⁴³ but is much better than that of F-Gr/Gr FET PD,²⁹ Gr/Au photoconductive PD,⁴⁴ and other Gr/Si photodiodes.⁴² On the other hand, under DUV light illumination, most of the parameters listed in the table are better than those of F-Gr/Gr FET PD.²⁹ These comparisons verify that the present F-Gr/Si dual-mode PD may be potentially important in some optoelectronic devices.

Even though our experimental result has shown that the fluorine atoms successfully formed chemical bonding with graphene, the formation of F-Gr is not a spontaneous chemical process at low temperature (less than 300 K) in that the free energy difference for all F-Gr with different F coverage is larger or at least comparable to 0 eV (Figure 7a). However, when the

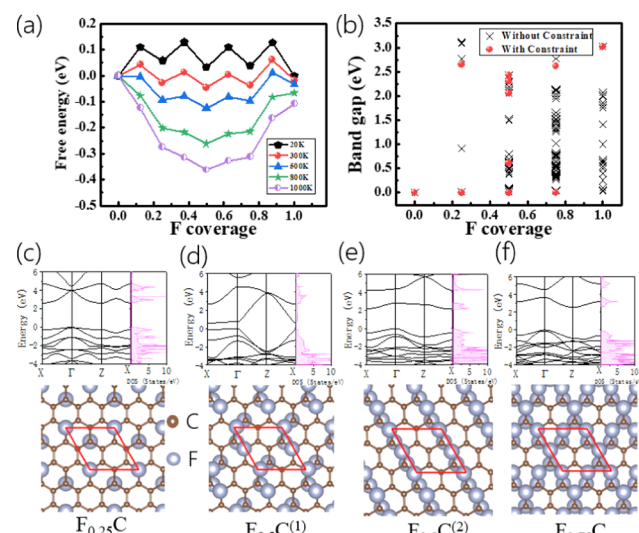


Figure 7. (a) Formation energies for F doping at different concentrations. (b) Theoretical band gaps of the F-doped Grs with different F concentrations. Energy and DOS of the typical structures: $\text{F}_{0.25}\text{C}$ (c), $\text{F}_{0.5}\text{C}^{(1)}$ (d), $\text{F}_{0.5}\text{C}^{(2)}$ (e), and $\text{F}_{0.75}\text{C}$ (f).

Table 1. Comparison of the Key Metrics of the Dual-Mode F-Gr/Si PD with Other F-Gr- and Gr-Based PD

device structure and applied voltage	wavelength, λ (nm)	$I_{\text{light}}/I_{\text{dark}}$ ratio	R (A W^{-1})	D^* (Jones)	τ_r/τ_f	refs
F-Gr/Si photoconductive PD ($V_{\text{bias}} = 5 \text{ V}$)	254		2.6×10^4	6.0×10^9	5.2/5.9 ms	this work
	650		1.9×10^7	4.4×10^{12}		
	1550		39	9.0×10^6		
F-Gr/Si photodiode PD ($V_{\text{bias}} = 0 \text{ V}$)	254	3.6×10^3	1.9×10^{-2}	1.3×10^{10}	6.3/9.7 μs	this work
	650	2.0×10^5	0.334	2.3×10^{11}		
	1550	8.0×10^2	6.3×10^{-3}	4.3×10^9		
F-Gr/Gr FET PD ($V_{\text{DS}} = 1 \text{ V}$, $V_{\text{GS}} = 28 \text{ V}$)	255		1.4×10^3	4.0×10^{10}	80 ms/0.20 s	29
	532		5.5×10^2	2.6×10^{10}		
	1319		1.7×10^2	1.2×10^{10}		
Gr/Si photoconductive PD ($V_{\text{bias}} = 5 \text{ V}$)	632		1.0×10^4		<0.1 ms	36
	1550		0.23		<0.1 ms	
Gr/Si photodiode PD ($V_{\text{bias}} = 0 \text{ V}$)	890	1.0×10^7	0.73	4.1×10^{13}	0.3/0.8 ms	43
Gr/Si photodiode PD ($V_{\text{bias}} = -2 \text{ V}$)	850	$>1.0 \times 10^4$	0.44	7.7×10^9	1.2/3.0 ms	42
Gr/Au photoconductive PD ($V_{\text{bias}} = 10 \text{ V}$)	1550		83	$\sim 10^8$	0.6/0.6 μs	44
Gr/Ge photoconductive PD ($V_{\text{bias}} = 1 \text{ V}$)	532		66		5.6/3.5 ms	49
	1550		2.0×10^{-3}			

reaction temperature is increased to 500, 800, or 1000 K, the free energy difference will be considerably reduced to less than 0 eV, indicative of a spontaneous fluorination process at a relatively high temperature (prior to calculation, the number of configurations is reduced from 3^8 to 35 after thorough consideration of both structural recognition and energetic preference, please see more detailed information in the Supporting Information). It is comprehensible that configuration entropy will enhance the structural stabilities of the partially fluorinated Gr and prevent the phase separation into the pure Gr or fully fluorinated Gr as the temperature increases, where the structural diversity of partially fluorinated Gr may further induce a variety of optical properties. To unveil the reason behind the broadband sensitivity of the F-Gr/Si device, we then calculated the band structure and the density of state (DOS) of F-Gr with different doping concentrations (Figure 7b). Figures S8 and 7c show six different isomers for $F_{0.25}C$ and band gaps as a function of different F coverage, respectively. It is found that the band gap of F-Gr is highly dependent on not only F coverage but also isomer structures. Gr without F doping has a band gap of 0 eV; however, once 20% of F atoms were doped, total of six different band gaps ranging from 0 to 3.1 eV corresponding to different isomer structures were induced (Figure 7c). Similar band gap opening was also observed on other doping levels including $F_{0.5}C$ and $F_{0.75}C$ (Figure 7d–f). Considering the complicity of the fluorination in the RIE chamber and poor controllability of the F doping levels, it is highly challenging to figure out the exact microstructure of F-Gr. In spite of this difficulty, we believe that the enhanced responsivity of the F-Gr/Si-heterojunction-based PD in the UV and NIR region should be ascribed to the opening of the band gap: due to the heterogeneity of the fluorine doping, F-Gr with different F coverages as well as band gaps may coexist in the as-obtained F-Gr layer. Such a wide range of distribution of the band gap due to different configurations can facilitate the wide-spectra absorption of the UV light, visible light, and NIR light, leading to broadband photoresponse in the region from DUV to NIR.

CONCLUSIONS

In summary, F-Gr has been realized by SF_6 plasma treatment of the CVD-grown Gr and a dual-mode broadband PD based on F-Gr/Si heterojunction was fabricated. The photoconductive PD showed excellent weak light detection ability over a broadband spectral region from UV–NIR, with the highest responsivity of 1.9×10^7 A W^{-1} for a 650 nm incident light at an intensity of 31 nW cm^{-2} . Moreover, in photodiode mode, the F-Gr/Si heterojunction PD showed a high I_{light}/I_{dark} ratio (2.0×10^5) and a fast response speed (6.3 μs for rise time and 9.7 μs for fall time) at 650 nm light. Compared with Gr/Si-based PD, the responsivity in both UV and NIR regions was remarkably enhanced, which was ascribed to the opening of the band gap by fluorination. This dual-mode PD enabled the simultaneous weak light detection and fast photodetection, which may find potential application in future optoelectronic devices and systems.

EXPERIMENTAL SECTION

Fluorinated Graphene (F-Gr) Growth. The Gr was synthesized by a CVD approach using Cu as a growth foil. For the fluorination of Gr, a piece of CVD-grown Gr film on copper foils was transferred into a reactive ion-etching system (RIE, IMECAS ME-3A). A mixed gas of SF_6 (5 sccm) and He (2 sccm) was used as the etching gas, and the

chamber pressure was set to 5 Pa. After reacting for 20 s under 13 V direct current bias, 5 W forward power and 1 W reflection power, F-Gr was obtained on the oxygen free copper foil.

Device Fabrication. A precleaned lightly doped n-type Si ($1-10 \Omega \text{ cm}$)/ SiO_2 (300 nm) was used as the substrate. Ten nanometers of Cr/50 nm Au bimetal electrode pairs with the channel width of 30 μm were deposited onto the substrate through photolithography and electron beam evaporation process. Photolithography was then performed again to protect the electrode area with photoresist. The substrate was then immersed in buffered oxide etch solution ($HF/NH_4F = 1:6$) for 5 min to etch away the unprotected SiO_2 . Al film was then deposited onto the substrate by e-beam evaporation and the thickness was recorded by a quartz crystal oscillator. With a higher chamber pressure of 1×10^{-2} Pa and a slower evaporation rate of 0.01 \AA s^{-1} , the as-deposited Al film will be spontaneously oxidized and form the AlO_x passivation layer. The as-obtained F-Gr was then transferred onto the substrate through the traditional wetting transfer process and further patterned by photolithography.⁴⁵ F-Gr outside the Cr/Au electrodes was removed by the following O_2 plasma etching. Eutectic In:Ga alloy was finally pasted onto the reverse side of the Si substrate for Ohmic contact with the bottom electrode.

Device Measurement and Characterization. The morphology was characterized using field-emission scanning electron microscope (FESEM, Hitachi SU8020). X-ray photoelectron (XPS) spectra were recorded on a Thermo ESCALAB250 X-ray photoelectron spectroscopy. Raman analysis was conducted using a microscopic confocal laser Raman spectrometer (HR Evolution Horiba) with a 532 nm laser source. Optoelectronic characterizations were carried out using a semiconductor characterization system (Keithley 4200-SCS) equipped with a broadband monochromator (SP 2150, Princeton Co.). Laser diodes with different wavelengths (254 and 650 nm, Tanon UV-100, 1550 nm, Thorlabs M1550L3) were also used as illumination sources.

The First-Principles Calculations. The first-principles calculations were performed using the Vienna ab initio simulation package,⁴⁶ where the projected augmented-wave⁴⁷ method was adopted with the exchange–correlation functional in the form of Perdew–Burke–Ernzerhof approximation.⁴⁸ The atomic positions and the cell parameters of the candidates were fully relaxed until the energy differences were less than 0.0001 eV. The cutoff energy of the plane wave was set to be 480 eV. The k meshes are distributed in reciprocal space with an average interval of 0.5\AA^{-1} .

The formation energies of the given configurations are calculated as

$$E_{\text{form}}(FxC) = E(FxC) - xE(FC) - (1-x)E(C)$$

where x is the coverage of F atoms on Gr and $E(FxC)$, $E(FC)$, and $E(C)$ are the total energies of the systems of partially/fully fluorinated Gr and pure Gr, respectively. To consider the temperature effect, the free energy differences of the systems are calculated as follows

$$E_{\text{free}}(FxC) = -kT \ln \sum_i g_i \exp(-E_{\text{form}}^i/kT)$$

where k is the Boltzmann constant, T is the temperature, g_i is the multiplicity of the specific configuration with the same coverage of F atoms.

ASSOCIATED CONTENT

Supporting Information

The Supporting Information is available free of charge on the ACS Publications website at DOI: 10.1021/acsami.9b04389.

Structural diversity of F-Gr, calculation of NEP, D^* , and EQE, $I-V$ curves of Gr and F-Gr in dark, schematic illustration of the fabrication of the F-Gr/Si dual-mode photodetector, XPS spectra of AlO_x passivation layer, response time of the F-Gr/Si photoconductive photodetector, measurement of the NEP, time-dependent response of F-Gr/Si- and Gr/Si-based photodetectors

upon 650 nm light, six typical structures with F coverage (PDF)

AUTHOR INFORMATION

Corresponding Authors

*E-mail: cywu@hfut.edu.cn (C.-Y.W.).

*E-mail: chao.xie@hfut.edu.cn (C.X.).

*E-mail: luolb@hfut.edu.cn (L.-B.L.).

*E-mail: jhliao@scut.edu.cn (J.H.L.).

ORCID

Xiao-Bao Yang: 0000-0001-8851-1988

Chao Xie: 0000-0003-4451-767X

Lin-Bao Luo: 0000-0001-8651-8764

Author Contributions

§J.-Y.X. and J.-S.Y. contributed equally to this work.

Notes

The authors declare no competing financial interest.

ACKNOWLEDGMENTS

This work is financially supported by the Natural Science Foundation of China (NSFC Nos. 61675062, 61575059, and 21501038), the Fundamental Research Funds for the Central Universities (JZ2018HGFB027, JZ2018HGXC0001, and JZ2018HGTA0220), and the Open Foundation of Key Laboratory of Advanced Functional Materials and Devices of the Anhui Province (Grant No. 4500-411104/011).

REFERENCES

- (1) Novoselov, K. S.; Geim, A. K.; Morozov, S. V.; Jiang, D.; Zhang, Y.; Dubonos, S. V.; Grigorieva, I. V.; Firsov, A. A. Electric Field Effect in Atomically Thin Carbon Films. *Science* **2004**, *306*, 666–669.
- (2) Wang, F.; Zhang, Y.; Tian, C.; Girit, C.; Zettl, A.; Crommie, M.; Shen, Y. R. Gate-Variable Optical Transitions in Graphene. *Science* **2008**, *320*, 206–209.
- (3) Bolotin, K. I.; Sikes, K. J.; Jiang, Z.; Klima, M.; Fudenberg, G.; Hone, J.; Kim, P.; Stormer, H. L. Ultrahigh Electron Mobility in Suspended Graphene. *Solid State Commun.* **2008**, *146*, 351–355.
- (4) Zeng, L. H.; Wang, M. Z.; Hu, H.; Nie, B.; Yu, Y. Q.; Wu, C. Y.; Wang, L.; Hu, J. G.; Xie, C.; Liang, F. X.; Luo, L. B. Monolayer Graphene/Germanium Schottky Junction as High-Performance Self-Driven Infrared Light Photodetector. *ACS Appl. Mater. Interfaces* **2013**, *5*, 9362–9366.
- (5) Hu, M.; Yan, Y.; Huang, K.; Khan, A.; Qiu, X.; Xu, D.; Zhang, H.; Yu, X.; Yang, D. Performance Improvement of Graphene/Silicon Photodetectors Using High Work Function Metal Nanoparticles with Plasma Effect. *Adv. Opt. Mater.* **2018**, *6*, No. 1701243.
- (6) Yavuz, S.; Loran, E. M.; Sarkar, N.; Fenning, D. P.; Bandaru, P. R. Enhanced Environmental Stability Coupled with a 12.5% Power Conversion Efficiency in an Aluminum Oxide-Encapsulated n-Graphene/p-Silicon Solar Cell. *ACS Appl. Mater. Interfaces* **2018**, *10*, 37181–37187.
- (7) Li, W.; Chen, B.; Meng, C.; Fang, W.; Xiao, Y.; Li, X.; Hu, Z.; Xu, Y.; Tong, L.; Wang, H.; Liu, W.; Bao, J.; Shen, Y. Ultrafast All-Optical Graphene Modulator. *Nano Lett.* **2014**, *14*, 955–959.
- (8) Sun, Z.; Popa, D.; Hasan, T.; Torrisi, F.; Wang, F.; Kelleher, E. J. R.; Travers, J. C.; Nicolosi, V.; Ferrari, A. C. A Stable, Wideband Tunable, Near Transform-Limited, Graphene-Mode-Locked, Ultrafast Laser. *Nano Res.* **2010**, *3*, 653–660.
- (9) Nair, R. R.; Blake, P.; Grigorenko, A. N.; Novoselov, K. S.; Booth, T. J.; Stauber, T.; Peres, N. M. R.; Geim, A. K. Fine Structure Constant Defines Visual Transparency of Graphene. *Science* **2008**, *320*, 1308.
- (10) Luo, L. B.; Xie, C.; Wang, X. H.; Yu, Y. Q.; Wu, C. Y.; Hu, H.; Zhou, K. Y.; Zhang, X. W.; Jie, J. S. Surface plasmon resonance

enhanced highly efficient planar silicon solar cell. *Nano Energy* **2014**, *9*, 112–120.

(11) Mueller, T.; Xia, F.; Avouris, P. Graphene Photodetectors for High-speed Optical Communications. *Nature Photon.* **2010**, *4*, 297–301.

(12) McCann, E. Asymmetry Gap in the Electronic Band Structure of Bilayer Graphene. *Phys. Rev. B* **2006**, *74*, No. 161403.

(13) Chen, Z.; Lin, Y.; Rooks, M. J.; Avouris, P. Graphene Nano-ribbon Electronics. *Phys. E* **2007**, *40*, 228–232.

(14) Han, M. Y.; Özyilmaz, B.; Zhang, Y.; Kim, P. Energy Band-Gap Engineering of Graphene Nanoribbons. *Phys. Rev. Lett.* **2007**, *98*, No. 206805.

(15) Lin, Y.-M.; Perebeinos, V.; Chen, Z.; Avouris, P. Electrical Observation of Subband Formation in Graphene Nanoribbons. *Phys. Rev. B* **2008**, *78*, No. 161409.

(16) Li, X.; Wang, X.; Zhang, L.; Lee, S.; Dai, H. Chemically Derived, Ultrasoft Graphene Nanoribbon Semiconductors. *Science* **2008**, *319*, 1229–1232.

(17) Wang, X.; Sun, G.; Routh, P.; Kim, D.-M.; Huang, W.; Chen, P. Heteroatom-Doped Graphene Materials: Syntheses, Properties and Applications. *Chem. Soc. Rev.* **2014**, *43*, 7067–7098.

(18) Wu, T.; Shen, H.; Sun, L.; Cheng, B.; Liua; Shen, J. Nitrogen and Boron Doped Monolayer Graphene by Chemical Vapor Deposition Using Polystyrene, Urea and Boric Acid. *New J. Chem.* **2012**, *36*, 1385–1391.

(19) Friedman, A. L.; Cress, C. D.; Schmucker, S. W.; Robinson, J. T.; van, O. M. J. t Erve. Electronic Transport and Localization in Nitrogen-Doped Graphene Devices Using Hyperthermal Ion Implantation. *Phys. Rev. B* **2016**, *93*, No. 161409.

(20) Zhang, H.; Fan, L.; Dong, H.; Zhang, P.; Nie, K.; Zhong, J.; Li, Y.; Guo, J.; Sun, X. Spectroscopic Investigation of Plasma-Fluorinated Monolayer Graphene and Application for Gas Sensing. *ACS Appl. Mater. Interfaces* **2016**, *8*, 8652–8661.

(21) Nair, R. R.; Ren, W.; Jalil, R.; Riaz, I.; Kravets, V. G.; Britnell, L.; Blake, P.; Schedin, F.; Mayorov, A. S.; Yuan, S.; Katsnelson, M. I.; Cheng, H. M.; Strupinski, W.; Bulusheva, L. G.; Okotrub, A. V.; Grigorieva, I. V.; Grigorenko, A. N.; Novoselov, K. S.; Geim, A. K. Fluorographene: A Two-Dimensional Counterpart of Teflon. *Small* **2010**, *6*, 2877–2884.

(22) Zhang, X.; Hsu, A.; Wang, H.; Song, Y.; Kong, J.; Dresselhaus, M. S.; Palacios, T. Impact of Chlorine Functionalization on High-Mobility Chemical Vapor Deposition Grown Graphene. *ACS Nano* **2013**, *7*, 7262–7270.

(23) Poh, H. L.; Šimek, P.; Sofer, Z.; Pumera, M. Sulfur-Doped Graphene via Thermal Exfoliation of Graphite Oxide in H₂S, SO₂, or CS₂ Gas. *ACS Nano* **2013**, *7*, 5262–5272.

(24) Avouris, P. Graphene: Electronic and Photonic Properties and Devices. *Nano Lett.* **2010**, *10*, 4285–4294.

(25) Samarakoon, D. K.; Chen, Z.; Nicolas, C.; Wang, X. Structural and Electronic Properties of Fluorographene. *Small* **2011**, *7*, 965–969.

(26) Leenaerts, O.; Peelaers, H.; Hernández-Nieves, A. D.; Partoens, B.; Peeters, F. M. First-Principles Investigation of Graphene Fluoride and Graphene. *Phys. Rev. B* **2010**, *82*, No. 195436.

(27) Zhang, H.; Fan, L.; Dong, H.; Zhang, P.; Nie, K.; Zhong, J.; Li, Y.; Guo, J.; Sun, X. Spectroscopic Investigation of Plasma-Fluorinated Monolayer Graphene and Application for Gas Sensing. *ACS Appl. Mater. Interfaces* **2016**, *8*, 8652–8661.

(28) Zhong, M.; Xu, D.; Yu, X.; Huang, K.; Liu, X.; Qu, Y.; Xu, Y.; Yang, D. Interface Coupling in Graphene/Fluorographene Heterostructure for High-Performance Graphene/Silicon Solar Cells. *Nano Energy* **2016**, *28*, 12–18.

(29) Du, S.; Lu, W.; Ali, A.; Zhao, P.; Shehzad, K.; Guo, H.; Ma, L.; Liu, X.; Pi, X.; Wang, P.; Fang, H.; Xu, Z.; Gao, C.; Dan, Y.; Tan, P.; Wang, H.; Lin, C.; Yang, J.; Dong, S.; Cheng, Z.; Li, E.; Yin, W.; Luo, J.; Yu, B.; Hasan, T.; Xu, Y.; Hu, W.; Duan, X. A Broadband Fluorographene Photodetector. *Adv. Mater.* **2017**, *29*, No. 1700463.

(30) Li, X.; Abe, T.; Esashi, M. Deep Reactive Ion Etching of Pyrex Glass Using SF₆ Plasma. *Sens. Actuators, A* **2001**, *87*, 139–145.

(31) Ferrari, A. C.; Meyer, J. C.; Scardaci, V.; Casiraghi, C.; Lazzeri, M.; Mauri, F.; Piscanec, S.; Jiang, D.; Novoselov, K. S.; Roth, S.; Geim, A. K. Raman Spectrum of Graphene and Graphene Layers. *Phys. Rev. Lett.* **2006**, *97*, No. 187401.

(32) Ni, Z.; Ma, L.; Du, S.; Xu, Y.; Yuan, M.; Fang, H.; Wang, Z.; Xu, M.; Li, D.; Yang, J.; Hu, W.; Pi, X.; Yang, D. Plasmonic Silicon Quantum Dots Enabled High-Sensitivity Ultrabroadband Photo-detection of Graphene-Based Hybrid Phototransistors. *ACS Nano* **2017**, *11*, 9854–9862.

(33) Eckmann, A.; Felten, A.; Mishchenko, A.; Britnell, L.; Krupke, R.; Novoselov, K. S.; Casiraghi, C. Probing the Nature of Defects in Graphene by Raman Spectroscopy. *Nano Lett.* **2012**, *12*, 3925–3930.

(34) Ferrari, A. C.; Basko, D. M. Raman Spectroscopy as a Versatile Tool for Studying the Properties of Graphene. *Nat. Nanotechnol.* **2013**, *8*, 235–246.

(35) Cançado, L. G.; Jorio, A.; Martins Ferreira, E. H.; Stavale, F.; Achete, C. A.; Capaz, R. B.; Moutinho, M. V. O.; Lombardo, A.; Kulmala, T. S.; Ferrari, A. C. Quantifying Defects in Graphene via Raman Spectroscopy at Different Excitation Energies. *Nano Lett.* **2011**, *11*, 3190–3196.

(36) Chen, Z.; Cheng, Z.; Wang, J.; Wan, X.; Shu, C.; Tsang, H. K.; Ho, H. P.; Xu, J.-B. High Responsivity, Broadband, and Fast Graphene/Silicon Photodetector in Photoconductor Mode. *Adv. Opt. Mater.* **2015**, *3*, 1207–1214.

(37) Xie, C.; You, P.; Liu, Z.; Li, L.; Yan, F. Ultrasensitive Broadband Phototransistors Based on Perovskite/Organic-Semiconductor Vertical Heterojunctions. *Light: Sci. Appl.* **2017**, *8*, No. e17023.

(38) Xu, H.; Wu, J.; Feng, Q.; Mao, N.; Wang, C.; Zhang, J. High Responsivity and Gate Tunable Graphene-MoS₂ Hybrid Phototransistor. *Small* **2014**, *10*, 2300–2306.

(39) Liu, F.; Kar, S. Quantum Carrier Reinvestment-Induced Ultrahigh and Broadband Photocurrent Responses in Graphene-Silicon Junctions. *ACS Nano* **2014**, *8*, 10270–10279.

(40) Luo, L.-B.; Hu, H.; Wang, X.-H.; Lu, R.; Zou, Y. F.; Yu, Y. Q.; Liang, F. X. A Graphene/GaAs Near-infrared Photodetector Enabled by Interfacial Passivation with Fast Response and High Sensitivity. *J. Mater. Chem. C* **2015**, *3*, 4723–4728.

(41) Zhang, Z.-X.; Zeng, L.-H.; Tong, X.-W.; Gao, Y.; Xie, C.; Tsang, Y.-H.; Luo, L.-B.; Wu, Y.-C. Ultrafast, Self-Driven, and Air-Stable Photodetectors Based on Multilayer PtSe₂/Perovskite Heterojunctions. *J. Phys. Chem. Lett.* **2018**, *9*, 1185–1194.

(42) An, X.; Liu, F.; Jung, Y. J.; Kar, S. Tunable Graphene–Silicon Heterojunctions for Ultrasensitive Photodetection. *Nano Lett.* **2013**, *13*, 909–916.

(43) Li, X.; Zhu, M.; Du, M.; Lv, Z.; Zhang, L.; Li, Y.; Yang, Y.; Yang, T.; Li, X.; Wang, K.; et al. High Detectivity Graphene-Silicon Heterojunction Photodetector. *Small* **2016**, *12*, 595–601.

(44) Chen, Z.; Li, X.; Wang, J.; Tao, L.; Long, M.; Liang, S. J.; Ang, L. K.; Shu, C.; Tsang, H. K.; Xu, J. B. Synergistic Effects of Plasmonics and Electron Trapping in Graphene Short-Wave Infrared Photodetectors with Ultrahigh Responsivity. *ACS Nano* **2017**, *11*, 430–437.

(45) Zhang, X.; Xie, C.; Jie, J.; Zhang, X.; Wu, Y.; Zhang, W. High-efficiency Graphene/Si Nanoarray Schottky Junction Solar Cells via Surface Modification and Graphene Doping. *J. Mater. Chem. A* **2013**, *1*, 6593–6601.

(46) Kresse, G.; Furthmüller, J. Efficiency of Ab-initio Total Energy Calculations for Metals and Semiconductors using a Plane-Wave Basis Set. *Comput. Mater. Sci.* **1996**, *6*, 15–50.

(47) Perdew, J. P.; Burke, K.; Ernzerhof, M. Generalized Gradient Approximation Made Simple. *Phys. Rev. Lett.* **1996**, *77*, 3865–3868.

(48) Kresse, G.; Joubert, D. From Ultrasoft Pseudopotentials to the Projector Augmented-wave Method. *Phys. Rev. B* **1999**, *59*, 1758–1775.

(49) Yang, F.; Cong, H.; Yu, K.; Zhou, L.; Wang, N.; Liu, Z.; Li, C.; Wang, Q.; Cheng, B. Ultrathin Broadband Germanium–Graphene Hybrid Photodetector with High Performance. *ACS Appl. Mater. Interfaces* **2017**, *9*, 13422–13429.